WILEY | Hindawi

Research Article

Numerical Simulation of a Floating Offshore Wind Turbine Incorporating an Electromagnetic Inerter-Based Device for Vibration Suppression and Wave Energy Conversion

Takehiko Asai [iD],[1] Shota Tsukamoto,[2] Yudai Nemoto,[3] Kenji Yoshimizu,[3] Urara Watanabe,[3] and Yoshihiro Taniyama[3]

[1]*Faculty of Engineering, Information and Systems, University of Tsukuba, Ibaraki, Japan*
[2]*Graduate School of Science and Technology, University of Tsukuba, Ibaraki, Japan*
[3]*Energy Systems Research and Development Center, Toshiba Energy Systems & Solutions Corporation, Kanagawa, Japan*

Correspondence should be addressed to Takehiko Asai; asai@kz.tsukuba.ac.jp

Offshore wind turbines (OWTs) are considered vital to the promotion of the development of renewable energy. Especially, floating OWTs can be deployed over a larger area than bottom-fixed OWTs. The floating OWTs, however, are vulnerable to vibration induced by disturbances and require a backup power supply in the case of power outage. On the one hand, various kinds of inerter-based devices have been proposed especially for vibration suppression of civil structures subjected to earthquake loadings. Recently, combined with electromagnetic devices, the inerter technologies have also been applied in the field of vibration energy harvesting such as point absorber wave energy converters. Thus, this paper proposes a novel floating OWT consisting of two bodies combined with inerter-based power take-off (PTO) devices which accomplishes vibration suppression and wave energy conversion at the same time. To investigate the vibration suppression and energy conversion capabilities of the proposed floating OWT with a variety of inerter-based PTO devices for ocean waves, numerical simulation studies employing WEC-Sim are conducted, and the performance of each system is compared for regular and irregular waves. Results show that the proposed floating OWT with the appropriately designed inerter-based PTO devices for the incident wave period has great potential for both vibration suppression and wave energy conversion in a specific frequency range.

1. Introduction

In recent decades, social demand for renewable energy has been increasing worldwide due to concerns about global warming and depletion of fossil fuels. Wind power is expected to be one of the most promising renewable energy sources; however, the land area on which wind turbines can be built is limited. Therefore, offshore wind turbines (OWTs), which can harness the vast offshore wind power, have been attracting attention [1–4], and the OWTs can be divided into two categories: bottom-fixed and floating OWTs. Although the development of the bottom-fixed OWTs has progressed considerably and its practical application has already been achieved, the bottom-fixed ones can

only be installed in waters up to about 50 meters deep. On the other hand, while the floating OWTs can be constructed in deeper waters, this type is still in the development stage, and there are many issues to be resolved for practical use.

One of the challenges of the floating OWTs to be addressed is the platform oscillation due to disturbances such as winds and waves. The same challenge can be seen in other civil structures subjected to earthquake loadings, and one of the strategies that have received the most attention in the field of structural vibration control recently is inerter [5, 6]. Originally, the inerter has been proposed by Smith [7] for vibration suppression in automobiles, and it produces a force proportional to the relative acceleration across its two terminals. The proportional constant between the force and

the relative acceleration is called inertance, which has the same physical unit as mass. It should be also noted that a large inertance can be realized easily through a ball screw or a rack and pinion from relatively small actual masses. Some inerter-based devices have already been applied to structures on the ground, and their applications to floating structures such as floating OWTs for vibration suppression are currently being studied. For example, Hu et al. [8] investigated the structural control performance of various kinds of inerter-based devices located at the nacelle part by using the FAST-SC code [9]. Zhang and Fitzgerald [10] installed a tuned mass damper-inerter (TMDI) at a location close to the tip of each blade for the mitigation of edgewise blade vibrations, and the TMDI and a tuned mass damper fluid-inerter (TMDFI) are also applied by Sarkar and Fitzgerald [11, 12]. Moreover, Zhang and Høeg [13] applied a rotational inertia double-tuned mass damper (RIDTMD) to a spar-type floating OWT. Ma et al. [14, 15] also examined the heave motion mitigation of a semisubmersible platform with the inerter technologies.

In addition, the inerter-based devices are applied to energy harvesting from vibrations of structures. So far, various kinds of inerter-based devices utilizing electromagnetic machines, such as electromagnetic inertial mass damper (EIMD) [16, 17], tuned inertial mass electromagnetic transducer (TIMET) [18, 19], and electromagnetic tuned inerter damper (E-TID) [20], have been developed. The EIMD consists of an inerter and a motor which are arranged in parallel. In the TIMET, a spring is connected to the EIMD to increase the energy absorption capability by taking advantage of the resonance effect of the inerter. The E-TID also consists of an inerter, a spring, and a motor as well as the TIMET, and the configuration of these elements are different from that of the TIMET: the spring and the motor are parallelized and the inerter is added in series with them. The energy harvesting potential of these devices were already shown, and particularly, a point absorber wave energy converter (WEC) employing the TIMET was introduced by the first author [21–24], showing that the mechanism of the TIMET was able to increase the wave energy absorption capability compared to the conventional WEC.

On the other hand, hybrid systems combining floating OWTs with various kinds of WECs [25, 26] such as torus [27–30], point floater [31], flap-type [32], oscillating water column [33], and wavestar-type [34, 35] have been proposed to harness both wind and wave energy. The common concept of these studies is to submerge WEC devices in water, and these devices are designed to mitigate the vibration of the floating OWT by absorbing the wave energy.

The aim of this paper is to present a novel spar-type floating OWT incorporating electromagnetic inerter-based devices as power take-off (PTO) systems to achieve further improvements in the performance of power generation and structural control for wave disturbances and to assess and compare these performances through numerical simulation studies using WEC-Sim (Wave Energy Converter SIMulator) [36]. Unlike the other WEC devices introduced in the literature, in the proposed system, the spar-type floating OWT is separated into two parts: the submerged body and

the superstructure, and is modeled as a two-degree-of-freedom (2DOF) in the heave direction. Then, these two bodies are connected by an elastic body, which can be modeled by a linear spring, and a PTO system combined with the inerter technologies. The spring stiffness is adjusted intentionally so that the second mode of the floating buoy itself amplifies the vibration, and then the PTO system is designed and installed so that the vibration energy is absorbed effectively and the amplified vibration being suppressed due to the second mode.

This article is organized as follows: first of all, analytical models for the proposed systems are developed and the response amplitude operators (RAOs) are calculated to examine the displacement response of the heave direction. Subsequently, numerical simulation studies for regular and irregular waves are carried out on a spar-type floating OWT model created based on the OC3 [37, 38] model, which is developed by the National Renewable Energy Laboratory (NREL). Finally, conclusions obtained from this research follow.

2. Problem Formulation

This section introduces the mechanism of the proposed floating OWT. Moreover, four types of PTO systems, three of which are coupled with electromagnetic inerter-based devices, for wave energy conversion and vibration suppression are reviewed briefly. Then, analytical models considering only the heave motion are derived, and the power generation of the PTO system is defined.

2.1. Floating OWT. The schematic diagram of the present floating OWT is illustrated in Figure 1. A typical spar-type floating OWT is shown in 1(a) where the whole structure consisting of a nacelle, a tower, and a platform can be modeled as a single rigid body. Also, any additional damping devices are not installed on the model shown in Figure 1(a). Generally, the natural period of a spar-type OWT in the heave direction is much longer than the wave period to avoid the resonance with incident waves. While as can be seen in Figure 1(b), the floating OWT proposed in this research is developed by separating the conventional floating OWT into two parts, submerged body and superstructure. The submerged body is a hollow platform and the superstructure is composed of the nacelle, tower, and platform. Part of the tower of the superstructure reaches into the interior of the hollow platform, and these two parts are connected by an elastic body and the PTO system, allowing each part behaves separately in the heave direction. The inherent damping also exists between the two parts. The concept of this floating OWT is developing a system consisting of two separate structures, which can be modeled as a 2DOF system in the heave direction. The proposed system is designed so that its second mode matches with the period of the incident waves. Then, the vibration energy excited resonantly in the second mode is absorbed by the PTO systems to harvest sufficient electrical energy from wave-induced vibration and to suppress the response of the floating OWT simultaneously without amplification due to the second mode.
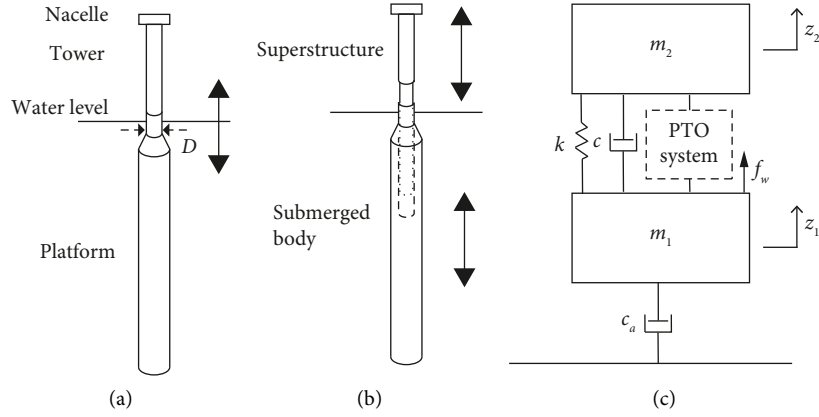
FIGURE 1: Floating offshore wind turbine: (a) schematic illustration of a spar-type floating offshore wind turbine, (b) schematic illustration of the separated system, and (c) analytical model of the separated system.

The analytical model considering only the heave motion is shown in Figure 1(c). The displacements of the submerged body and the superstructure are defined as z_1 and z_2, respectively. Let the force produced by the PTO system be f_e, then the equations of motion of the submerged body and the superstructure are given as follows:

$$m_1 \ddot{z}_1 + c(\dot{z}_1 - \dot{z}_2) + c_a \dot{z}_1 + k(z_1 - z_2) = f_e + f_w, \quad (1)$$

and

$$m_2 \ddot{z}_2 - c(\dot{z}_1 - \dot{z}_2) - k(z_1 - z_2) = -f_e, \quad (2)$$

respectively, where m_1 is the mass of the submerged body, m_2 is the mass of the superstructure, k is the stiffness of the elastic body inserted between the submerged body and the superstructure, c is the unavoidable inherent damping coefficient caused between them, and c_a is the additional linear damping coefficient considered in [38]. Furthermore, f_w is the hydrodynamic force acting of the submerged body, which is described based on the linear potential wave theory [39, 40] by

$$f_w = f_a + f_b + f_c, \quad (3)$$

where f_a is the excitation force, f_b is the hydrodynamic force due to buoyancy, and f_c is the radiation force.

The relationship between the excitation force in the heave direction f_a and the amplitude of the incident wave $a(t)$ is given in the frequency domain using a transfer function $F(\omega)_{a,3}$ as

$$\hat{f}_a(\omega) = F_{a,3}(\omega)\hat{a}(\omega), \quad (4)$$

where $\hat{f}(\omega)$ denotes the Fourier transform of a function $f(t)$.

Assume that the submerged body is a tapered cylinder as shown in Figure 1 and its diameter at the water level is D. Thus, the hydrodynamic force f_b becomes a linear function of z_1 as

$$f_b = -K_w z_1, \quad (5)$$

where

$$K_w = \rho g \pi \left(\frac{D}{2}\right)^2, \quad (6)$$

and g is gravitational acceleration and ρ is the sea water density.

Finally, the radiation force f_c is given by

$$\hat{f}_c = -A_{33}(\omega)\hat{\ddot{z}}_1 - B_{33}(\omega)\hat{\dot{z}}_1, \quad (7)$$

where $A_{33}(\omega)$ and $B_{33}(\omega)$ are the added mass and the radiation damping in the heave direction of the submerged body.

2.2. PTO Systems.
To absorb the vibration energy and convert it to electrical energy, PTO systems are installed between the submerged body and the superstructure of the floating OWT introduced above. This paper investigates the three kinds of inerter-based electromagnetic devices, i.e., EIMD, TIMET, and E-TID. For comparison, an ordinary PTO system without an inerter mechanism is examined as well. The models of these four PTO systems are depicted in Figure 2.

2.2.1. Electromagnetic Device without Inerter (2DOF).
When the PTO system without an inerter as shown in Figure 2(a) is installed between the submerged body and the superstructure, the device force becomes

$$f_e = C_{\text{PTO}}(\dot{z}_2 - \dot{z}_1), \quad (8)$$

where C_{PTO} is the damping coefficient of the motor for the PTO system. Thus, equations (1) and (2) can be written as
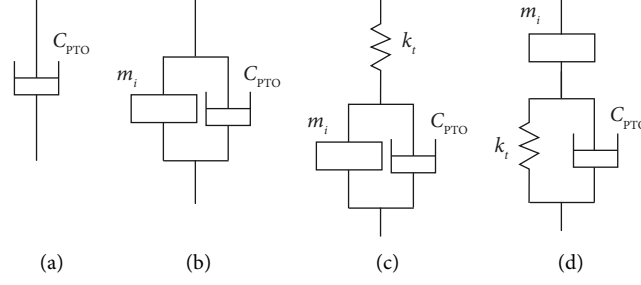
FIGURE 2: PTO system models: (a) electromagnetic device without inerter, (b) electromagnetic inertial mass damper (EIMD), (c) tuned inertial mass electromagnetic transducer (TIMET), and (d) electromagnetic tuned inerter damper (E-TID).

$$m_1 \ddot{z}_1 + (c + c_a + C_{\text{PTO}})\dot{z}_1 - (c + C_{\text{PTO}})\dot{z}_2 + kz_1 - kz_2 = f_a + f_b + f_c,$$
$$m_2 \ddot{z}_2 - (c + C_{\text{PTO}})\dot{z}_1 + (c + C_{\text{PTO}})\dot{z}_2 - kz_1 + kz_2 = 0,$$
(9)

respectively.

Substituting, equations (4), (5), and (7) and taking the Fourier transform of these equations gives

$$\mathbf{X}(\omega)\begin{bmatrix} \hat{z}_1 \\ \hat{z}_2 \end{bmatrix} = \begin{bmatrix} F_{a,3}(\omega) \\ 0 \end{bmatrix}\hat{a}(\omega), \quad (10)$$

where each element of $\mathbf{X}$ is given as

$$X_{11} = k + K_w - \omega^2 (m_1 + A_{33}(\omega))$$
$$+ j\omega (c + c_a + C_{\text{PTO}} + B_{33}(\omega)),$$
$$X_{12} = -k - j\omega (c + C_{\text{PTO}}), \quad (11)$$
$$X_{21} = X_{12},$$
$$X_{22} = k - \omega^2 m_2 + j\omega (c + C_{\text{PTO}}).$$

This case is referred to 2DOF model in this article.

2.2.2. Electromagnetic Inertial Mass Damper (EIMD).
Then, the EIMD [16, 17] shown in Figure 2(b) is applied. In the same way as the 2DOF model, the device force is given by

$$f_e = m_i (\ddot{z}_2 - \ddot{z}_1) + C_{\text{PTO}} (\dot{z}_2 - \dot{z}_1). \quad (12)$$

The system still can be expressed as a 2DOF system, and the equations of motion are given by

$$(m_1 + m_i)\ddot{z}_1 - m_i \ddot{z}_2 + (c + c_a + C_{\text{PTO}})\dot{z}_1 - (c + C_{\text{PTO}})\dot{z}_2 + kz_1 - kz_2 = f_a + f_b + f_c,$$
$$-m_i \ddot{z}_1 + (m_2 + m_i)\ddot{z}_2 - (c + C_{\text{PTO}})\dot{z}_1 + (c + C_{\text{PTO}})\dot{z}_2 - kz_1 + kz_2 = 0,$$
(13)

respectively.

The Fourier transform of these equations has the same form as equation (10); however, each element of $\mathbf{X}$ is given as

$$X_{11} = k + K_w - \omega^2 (m_1 + m_i + A_{33}(\omega))$$
$$+ j\omega (c + c_a + C_{\text{PTO}} + B_{33}(\omega)),$$
$$X_{12} = -k + \omega^2 m_i - j\omega (c + C_{\text{PTO}}), \quad (14)$$
$$X_{21} = X_{12},$$
$$X_{22} = k - \omega^2 (m_2 + m_i) + j\omega (c + C_{\text{PTO}}).$$

2.2.3. Tuned Inertial Mass Electromagnetic Transducer (TIMET).
A model for the floating OWT with the TIMET [18, 19] shown in Figure 2(c) is developed. Let the deformation of the inerter be z_i and consider the equilibrium

of force in the TIMET. Then, the force produced by the TIMET can be expressed as

$$f_e = k_t (z_2 - z_1 - z_i) = m_i \ddot{z}_i + C_{\text{PTO}}\dot{z}_i. \quad (15)$$

Substituting (15) into equations (1) and (2) yields

$$m_1 \ddot{z}_1 + (c + c_a)\dot{z}_1 - c\dot{z}_2 + (k + k_t)z_1$$
$$- (k + k_t)z_2 + k_t z_i = f_a + f_b + f_c, \quad (16)$$

and

$$m_2 \ddot{z}_2 - c\dot{z}_1 + c\dot{z}_2 - (k + k_t)z_1 + (k + k_t)z_2 - k_t z_i = 0, \quad (17)$$

and rewriting equation (15) gives

$$m_i \ddot{z}_i + C_{\text{PTO}}\dot{z}_i + k_t z_1 - k_t z_2 + k_t z_i = 0. \quad (18)$$

Thus, the degree of freedom for this system becomes three.

Taking the Fourier transform of equations (16)–(18) gives

$$\mathbf{X} \begin{bmatrix} \hat{z}_1 \\ \hat{z}_2 \\ \hat{z}_i \end{bmatrix} = \begin{bmatrix} F_{a,3}(\omega) \\ 0 \\ 0 \end{bmatrix} \hat{a}(\omega), \qquad (19)$$

where each element of $\mathbf{X}$ is given as

$$\begin{aligned}
X_{11} &= k + k_t + K_w - \omega^2 (m_1 + A_{33}(\omega)) \\
&\quad + j\omega (c + c_a + B_{33}(\omega)), \\
X_{12} &= -(k + k_t) - j\omega c, \\
X_{13} &= k_t, \\
X_{21} &= X_{12}, \\
X_{22} &= k + k_t - \omega^2 m_2 + j\omega c, \\
X_{23} &= -k_t, \\
X_{31} &= X_{13}, \\
X_{32} &= X_{23}, \\
X_{33} &= k_t - \omega^2 m_i + j\omega C_{\text{PTO}}.
\end{aligned} \qquad (20)$$

2.2.4. Electromagnetic Tuned Inerter Damper (E-TID).

Finally, the E-TID [20] shown in Figure 2(d) is installed on the floating OWT. As in the previous TIMET case, the system becomes a three-degree-of-freedom model, and the device force for the E-TID is expressed as

$$f_e = k_t (z_2 - z_1 - z_i) + C_{\text{PTO}} (\dot{z}_2 - \dot{z}_1 - \dot{z}_i) = m_i \ddot{z}_i, \qquad (21)$$

where z_i is the displacement of the inerter as in the TIMET case. Then, the equations of motion are as follows:

$$m_1 \ddot{z}_1 + (c + c_a + C_{\text{PTO}}) \dot{z}_1 - (c + C_{\text{PTO}}) \dot{z}_2 + C_{\text{PTO}} \dot{z}_i + (k + k_t) z_1 - (k + k_t) z_2 + k_t z_i = f_a + f_b + f_c, \qquad (22)$$

$$m_2 \ddot{z}_2 - (c + C_{\text{PTO}}) \dot{z}_1 + (c + C_{\text{PTO}}) \dot{z}_2 - C_{\text{PTO}} \dot{z}_i - (k + k_t) z_1 + (k + k_t) z_2 - k_t z_i = 0, \qquad (23)$$

and

$$m_i \ddot{z}_i + C_{\text{PTO}} \dot{z}_1 - C_{\text{PTO}} \dot{z}_2 + C_{\text{PTO}} \dot{z}_i + k_t z_1 - k_t z_2 + k_t z_i = 0. \qquad (24)$$

The Fourier transform of equations (22)–(24) has the same form as equation (19), and each element of $\mathbf{X}$ is given as

$$\begin{aligned}
X_{11} &= k + k_t + K_w - \omega^2 (m_1 + A_{33}(\omega)) \\
&\quad + j\omega (c + c_a + C_{\text{PTO}} + B_{33}(\omega)), \\
X_{12} &= -(k + k_t) - j\omega (c + C_{\text{PTO}}), \\
X_{13} &= k_t + i\omega C_{\text{PTO}}, \\
X_{21} &= X_{12}, \\
X_{22} &= k + k_t - \omega^2 m_2 + j\omega (c + C_{\text{PTO}}), \\
X_{23} &= -k_t - j\omega C_{\text{PTO}}, \\
X_{31} &= X_{13}, \\
X_{32} &= X_{23}, \\
X_{33} &= k_t - \omega^2 m_i + j\omega C_{\text{PTO}}.
\end{aligned} \qquad (25)$$

2.3. Power Generation Objective.

To assess the power generation capability, the power generated by the PTO system is defined here. Let the back-EMF constant of the motor of the PTO system be K_e, and assume the relationship between the current and the voltage of the motor to be

$$i(t) = -\frac{v(t)}{R}, \qquad (26)$$

where R is the electrical resistance of the circuit including the internal resistance or coil resistance in the motor. Thus, the damping coefficient of the motor, C_{PTO}, is given by [41]

$$C_{\text{PTO}} = \frac{K_e^2}{R}. \qquad (27)$$

This equation shows that C_{PTO} is variable by controlling the electrical resistance.

The absorbed mechanical energy by the PTO system is defined as

$$P_a = \begin{cases} C_{\text{PTO}} (\dot{z}_1 - \dot{z}_2)^2, & \text{for 2DOF and EIMD,} \\ C_{\text{PTO}} \dot{z}_i^2, & \text{for TIMET and E-TID.} \end{cases} \qquad (28)$$

Strictly speaking, to calculate the generation power, the power loss caused by the internal resistance or coil resistance in the motor should be considered. However, with a motor of this size, the power loss is negligibly relative to the absorbed power. Therefore, for the sake of brevity, the power generation is defined as the absorbed energy, i.e.,

$$P_g = P_a. \tag{29}$$

Moreover, the average power generation from time 0 to t_f is defined as

$$\overline{P}_g = \frac{1}{t_f} \int_0^{t_f} P_g dt. \tag{30}$$

3. Numerical Simulation

In this section, numerical simulation studies are performed using WEC-Sim to evaluate the structural control performance and the wave energy conversion efficacy of the proposed system to various wave inputs. WEC-Sim is an open-source code developed in MATLAB/Simulink [42] for simulating the behaviors of WECs.

3.1. Parameters. The parameters for the spar-type floating OWT are decided based on the OC3 whose total length is 210 m developed by the NREL [37, 38] and are summarized in Table 1. Since the detailed shape of the OC3 platform is not given in the literature, this research assumes that the part that submerged in the water is a perfect cylinder except for the tapered portion of the platform and that the mass distribution of this part is uniform. These assumptions lead to an error in buoyancy; thus, the parameters in Table 1 are slightly different from the values in the literature to adjust the draft depth in static equilibrium state.

The transfer function vector for the wave excitation force $\mathbf{F}_a(\omega)$, added mass matrix $\mathbf{A}(\omega)$, and radiation damping matrix $\mathbf{B}(\omega)$ for the WEC-Sim simulation are produced by the WAMIT software [40].

3.2. PTO System Design. To examine the effect of the inertance and the damping coefficient of the inerter-based PTO systems shown in Figure 2 on the vibration response and power generation efficacy, three different values for m_i and C_{PTO}, respectively, are adopted, and then nine cases (Case A through Case I) summarized in Table 2 are applied for each PTO system. The stiffness of the spring k_t used in the TIMET and E-TID is fixed to a constant value and given in Table 2 as well. These values are determined by trial and error so that the response amplitude operator (RAO) [43] introduced later is suppressed to waves with a period of around 10.0 s successfully. Note that the 2DOF model have neither a spring nor an inerter; thus, for the 2DOF model, cases A, B, and C are identical, and similarly cases D, E, and F and cases G, H, and I are identical, respectively. Also note that the EIMD device does not have a spring.

3.3. Response Amplitude Operator (RAO). Prior to performing the analysis in WEC-Sim, the RAO [43] for the heave direction is derived here. The RAO is a transfer function showing the relationship between the incident wave amplitude and the response displacement amplitude in the

TABLE 1: Parameters for the floating OWT.

Parameter	Value
m_1	7,399,000 kg
m_2	697,460 kg
c	10,000 N/m
c_a	130,000 N/m
k	250,000 N/m
ρ	1,025 kg/m^{-3}
D	6.5 m

TABLE 2: Parameters for the PTO systems.

	k_t (N/m)	m_i (kg)	C_{PTO} (Ns/m)
Case A	200,000	200,000	70,000
Case B	200,000	300,000	70,000
Case C	200,000	400,000	70,000
Case D	200,000	200,000	100,000
Case E	200,000	300,000	100,000
Case F	200,000	400,000	100,000
Case G	200,000	200,000	130,000
Case H	200,000	300,000	130,000
Case I	200,000	400,000	130,000

frequency domain. Let the inverse of $\mathbf{X}(\omega)$ derived in the previous section be $\overline{\mathbf{X}}(\omega)$, then the RAO for the superstructure when the abovementioned four devices are installed on the floating OWT can be expressed as

$$\frac{|\hat{z}_2(\omega)|}{|\hat{a}(\omega)|} = |\overline{X}_{21}(\omega)F_{a,3}(\omega)|, \tag{31}$$

where $\overline{X}_{21}$ is the element of the second row and first column of $\overline{\mathbf{X}}(\omega)$.

The RAOs obtained from equation (31) are shown in Figure 3 as well as the single-degree-of-freedom (SDOF) model for comparison, in which the submerged body and superstructure are rigidly connected without any PTO systems, i.e., the original spar-type floating OWT, as shown in Figure 1(a). The mass of the SDOF model is assumed to be $m_1 + m_2$. Note that the RAOs for the SDOF model in all cases in Figure 3 are identical. As stated previously, for the 2DOF model, the RAOs for cases A, B, and C, cases D, E, and F, and cases G, H, and I are identical, respectively, because the 2DOF model does not have an inerter.

It is observed in Figure 3 that the 2DOF model increases the RAO compared to the SDOF model due to the excitation in the second mode as intended. Then, it can be confirmed that the floating OWT with the inerter-based PTO systems such as EIMD, TIMET, and E-TID have the potential of suppressing the RAO and that the effective period range depends on the inertance value. Especially, the TIMET and the E-TID work well and show better performance than the SDOF model in the specific period range due to the additional spring, while these PTO systems have a risk of increasing the RAO outside the intended period range. From these results, a mechanism that controls the inertance for the EIMD, TIMET, and E-TID according to the change of the incident wave period is considered very promising.
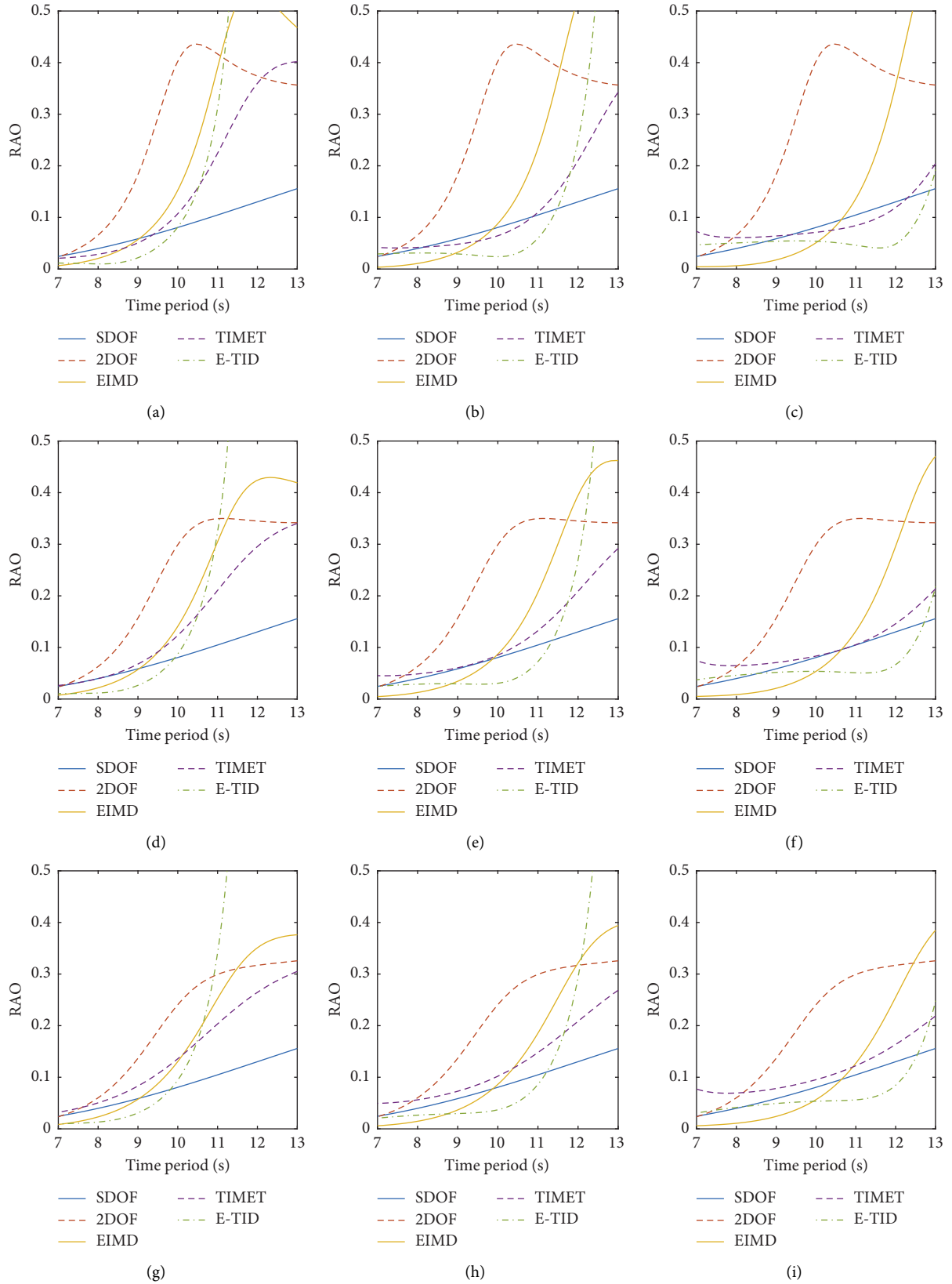
FIGURE 3: Comparison of RAO: (a) Case A ($m_i = 200,000$ kg and $C_{PTO} = 70,000$ Ns/m), (b) Case B ($m_i = 300,000$ kg and $C_{PTO} = 70,000$ Ns/m), (c) Case C ($m_i = 400,000$ kg and $C_{PTO} = 70,000$ Ns/m), (d) Case D ($m_i = 200,000$ kg and $C_{PTO} = 100,000$ Ns/m), (e) Case E ($m_i = 300,000$ kg and $C_{PTO} = 100,000$ Ns/m), (f) Case F ($m_i = 400,000$ kg and $C_{PTO} = 100,000$ Ns/m), (g), Case G ($m_i = 200,000$ kg and $C_{PTO} = 130,000$ Ns/m), (h) Case H ($m_i = 300,000$ kg and $C_{PTO} = 130,000$ Ns/m), and (i) Case I ($m_i = 400,000$ kg and $C_{PTO} = 130,000$ Ns/m).
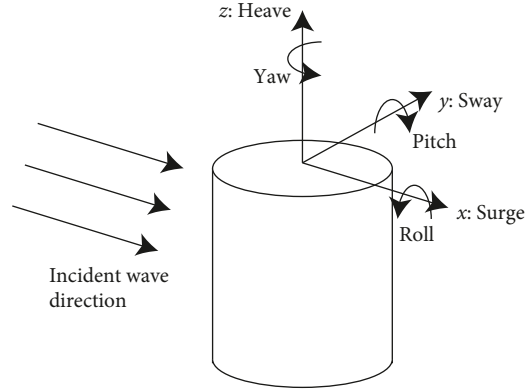
FIGURE 4: Coordinate system and incident wave direction.

TABLE 3: RMS response values and average power for the regular waves with a height of 6.0 m and a period of 9.0 s.

	Case	Heave ($\times 10^{-1}$ m)	Pitch ($\times 10^{-2}$ deg)	Surge ($\times 10^{-1}$ m)	Avg. power (kW)
SDOF		1.27	3.42	3.60	0
2DOF	A, B, and C	3.95	3.42	3.60	9.30
	D, E, and F	3.38	3.42	3.60	9.36
	G, H, and I	2.95	3.42	3.60	8.77
EIMD	A	1.24	3.42	3.60	2.23
	B	0.716	3.42	3.60	1.36
	C	0.413	3.42	3.60	0.911
	D	1.24	3.42	3.60	2.89
	E	0.760	3.42	3.60	1.83
	F	0.479	3.42	3.60	1.25
	G	1.25	3.42	3.60	3.36
	H	0.808	3.42	3.60	2.21
	I	0.547	3.42	3.60	1.55
TIMET	A	1.09	3.42	3.60	3.37
	B	1.04	3.42	3.60	2.18
	C	1.38	3.42	3.60	1.52
	D	1.46	3.42	3.60	4.44
	E	1.30	3.42	3.60	2.96
	F	1.52	3.42	3.60	2.09
	G	1.78	3.42	3.60	5.24
	H	1.56	3.42	3.60	3.60
	I	1.68	3.42	3.60	2.60
E-TID	A	0.489	3.42	3.60	0.815
	B	0.640	3.42	3.60	1.13
	C	1.16	3.42	3.60	1.36
	D	0.585	3.42	3.60	1.07
	E	0.645	3.42	3.60	1.47
	F	1.11	3.42	3.60	1.76
	G	0.676	3.42	3.60	1.25
	H	0.649	3.42	3.60	1.72
	I	1.06	3.42	3.60	2.05

3.4. Time History Analysis in WEC-Sim. Time history response analysis is conducted employing WEC-Sim here. The wave excitation force, added mass, and radiation damping obtained by WAMIT are used. Regular and irregular waves with a duration of 1000 s are input as incident waves. Although the proposed systems aim to suppress vibration of the floating OWT in the heave direction, the influences in other directions are examined. The analytical model developed for the WEC-Sim simulation studies is assumed to be symmetric; thus, without loss of generality, the analysis in WEC-Sim can be constrained to three directions: heave, pitch, and surge. For the simulation, the coordinates (x, y, z) of the center of gravity of the submerged body and the superstructure are set to $(0, 0, -89.9$ m$)$ and $(0, 0, 64.0$ m$)$, respectively, and the pitching moments of inertia are 42.3×10^8 kg·m^2 and 7.0×10^8 kg·m^2, respectively. Note that

TABLE 4: RMS response values and average power for the regular waves with a height of 6.0 m and a period of 10 s.

	Case	Heave ($\times 10^{-1}$ m)	Pitch ($\times 10^{-2}$ deg)	Surge ($\times 10^{-1}$ m)	Avg. power (kW)
SDOF		1.74	0.715	3.82	0
2DOF	A, B, and C	8.61	0.781	3.83	23.8
	D, E, and F	6.40	0.750	3.82	18.1
	G, H, and I	5.15	0.737	3.82	14.6
EIMD	A	3.28	0.721	3.82	7.02
	B	1.90	0.716	3.82	3.73
	C	1.11	0.715	3.82	2.25
	D	3.03	0.722	3.82	7.97
	E	1.88	0.717	3.82	4.68
	F	1.17	0.715	3.82	2.97
	G	2.81	0.722	3.82	8.16
	H	1.86	0.717	3.82	5.26
	I	1.24	0.716	3.82	3.51
TIMET	A	2.29	0.719	3.82	7.04
	B	1.38	0.716	3.82	3.74
	C	1.53	0.715	3.82	2.25
	D	2.64	0.721	3.82	7.98
	E	1.82	0.716	3.82	4.69
	F	1.78	0.715	3.82	2.97
	G	2.90	0.721	3.82	8.17
	H	2.18	0.717	3.82	5.26
	I	2.04	0.715	3.82	3.51
E-TID	A	1.74	0.715	3.82	1.45
	B	0.530	0.715	3.82	1.46
	C	1.16	0.715	3.82	1.46
	D	1.87	0.715	3.82	1.97
	E	0.669	0.715	3.82	1.97
	F	1.16	0.715	3.82	1.97
	G	2.02	0.715	3.82	2.40
	H	0.803	0.715	3.82	2.41
	I	1.15	0.715	3.82	2.41

the coordinate system in WEC-Sim is defined as shown in Figure 4, in which the origin is placed on the water line and the incident wave direction defined in the same direction as the x-axis is also depicted.

3.4.1. Regular Wave. To investigate the performance for different wave periods, regular waves with a period of 9.0 s, 10.0 s, and 11.0 s are used as incident waves. The wave height of these waves is set to 6.0 m. These conditions are determined with reference to various literature [37, 38, 43]. The RMS (root mean square) response values of the heave, pitch, and surge of the superstructure calculated by WEC-Sim for 1000 s are summarized as well as the average power generation calculated by equation (30) in Tables 3–5. In particular, the heave response ratio to the SDOF model and the power generation are compared in Figure 5. Moreover, the time histories for 100 s of the heave response and power generation for Case E to each input are compared in Figures 6–8, respectively.

From Tables 3–5 and Figure 5, the same trend as in Figure 3 can be confirmed for the heave direction, i.e., the inerter-based PTO systems show great potential for heave response reduction in the specific period range when the PTO parameters are appropriately designed. For example,

for the waves of period 10.0 s, cases C, F, and I of the EIMD, cases B and C of the TIMET, and cases of B, C, E, F, H, and I of the E-TID are superior to the SDOF model in the heave response. Especially, the PTO system utilizing the E-TID works better than the other systems in reducing the heave response when the parameters of the device are well matched to the incident wave period, while the E-TID has a risk of amplifying the heave response drastically to the unexpected incident wave period and is inferior to other schemes in power generation efficiency. Thus, it can be found out that the E-TID is very sensitive to the time period of the incident waves. This corresponds to the results reported in [44]. Hence, the inertance value of the E-TID should be designed carefully. Moreover, it can be found that the proposed systems utilizing an inerter have little effect on the responses in the pitch and surge directions. These results also show that a more effective system for vibration suppression over a wider period range can be developed if the inertance is variable and controllable based on the incident wave period. Also, it is observed that the power generation performance of the systems with the inerter-based PTOs is not as good as that of the 2DOF system, even when the response is reduced successfully. This is because the response reduction depends not only on energy absorption but also on the input energy

TABLE 5: RMS response values and average power for the regular waves with a height of 6.0 m and a period of 11.0 s.

	Case	Heave ($\times 10^{-1}$ m)	Pitch ($\times 10^{-2}$ deg)	Surge ($\times 10^{-1}$ m)	Avg. power (kW)
SDOF		2.25	6.82	3.77	0
2DOF	A, B, and C	8.86	6.82	3.77	14.3
	D, E, and F	7.44	6.82	3.77	14.0
	G, H, and I	6.38	6.82	3.77	12.9
EIMD	A	8.30	6.83	3.78	22.3
	B	5.00	6.82	3.77	11.6
	C	2.93	6.82	3.77	6.10
	D	6.50	6.83	3.77	18.6
	E	4.42	6.82	3.77	12.1
	F	2.83	6.82	3.77	7.28
	G	5.39	6.82	3.77	15.6
	H	3.97	6.82	3.77	11.6
	I	2.74	6.82	3.77	7.79
TIMET	A	4.79	6.82	3.77	14.1
	B	2.35	6.82	3.77	6.87
	C	1.80	6.82	3.77	3.65
	D	4.50	6.82	3.77	12.3
	E	2.83	6.82	3.77	7.47
	F	2.25	6.82	3.77	4.47
	G	4.34	6.82	3.77	10.5
	H	3.16	6.82	3.77	7.38
	I	2.62	6.82	3.77	4.89
E-TID	A	6.72	6.82	3.77	4.66
	B	1.28	6.82	3.77	2.38
	C	0.996	6.82	3.77	1.82
	D	6.99	6.82	3.77	6.45
	E	1.56	6.82	3.77	3.30
	F	1.10	6.82	3.77	2.53
	G	7.34	6.82	3.77	8.10
	H	1.84	6.82	3.77	4.15
	I	1.21	6.82	3.77	3.17

to the floating OWTs from the waves. As explained previously, the inerter-based PTOs are designed so that the response is reduced, leading to less input energy and less power generation. However, the proposed systems realize that wave energy conversion is not possible with the conventional SDOF model in addition to the response reduction.

The time histories of the heave response and the power generation for 100 s to each regular wave input are compared in Figures 6–8, respectively. Generally, the wave height is defined as the vertical distance between the crest and the trough of a wave, so it is equivalent to twice the amplitude of the sinusoidal wave. Taking this into account, the heave responses in time histories agree very well with the RAO, as shown in Figure 3.

3.4.2. JONSWAP Spectrum Wave. Then, irregular waves with the JONSWAP spectrum [43] are employed to evaluate the proposed system. The JONSWAP spectrum in WEC-Sim is defined as [36]

$$S_{JS}(f) = \frac{H_{1/3}^2}{4}\left(1 - 0.287\ln(\gamma)\right)\left(1.057 f_p\right)^4 f^{-5} \exp\left[-\frac{5}{4}\left(\frac{f_p}{f}\right)^4\right]\gamma^{\alpha}, \tag{32}$$
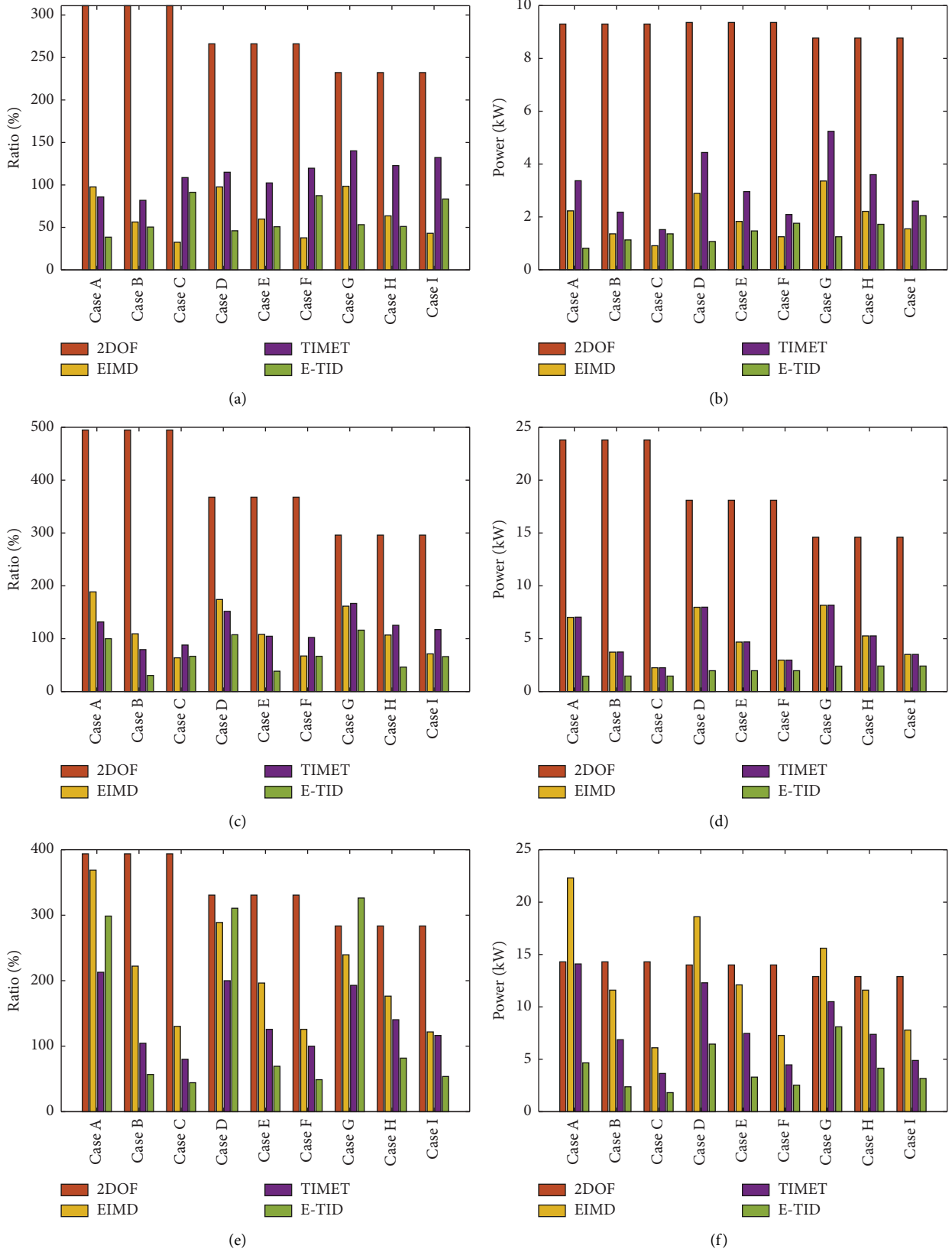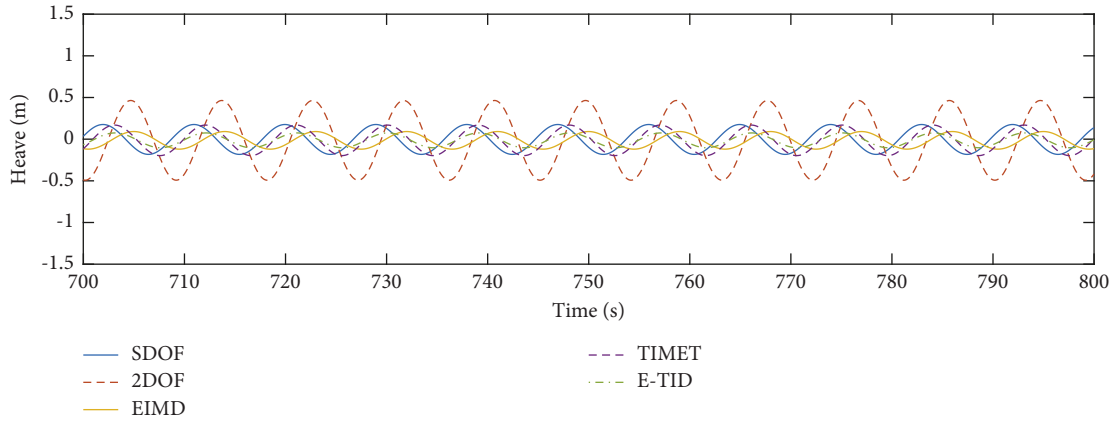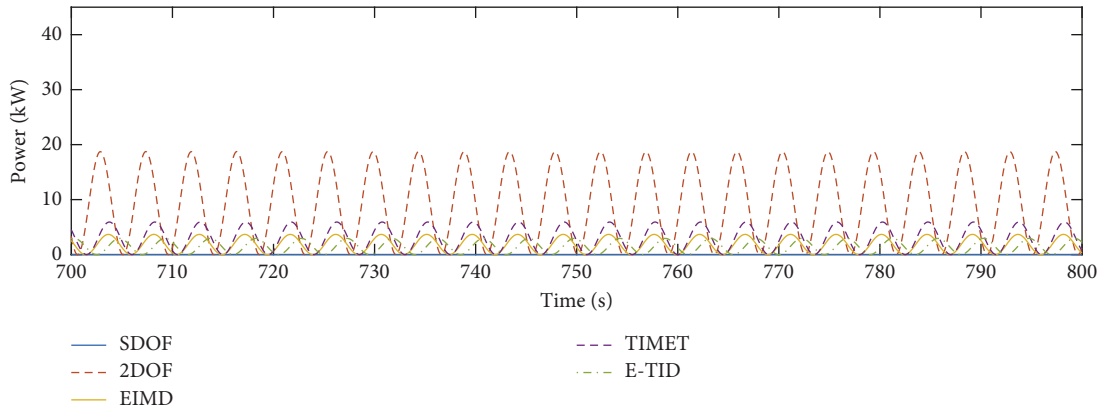
Figure 5: Comparisons of the RMS heave response ratio to the SDOF model and the average power generation for the regular waves: (a, b) with a height of 6.0 m and a period of 9.0 s, (c, d) with a height of 6.0 m and a period of 10.0 s, and (e, f) with a height of 6.0 m and a period of 11.0 s.
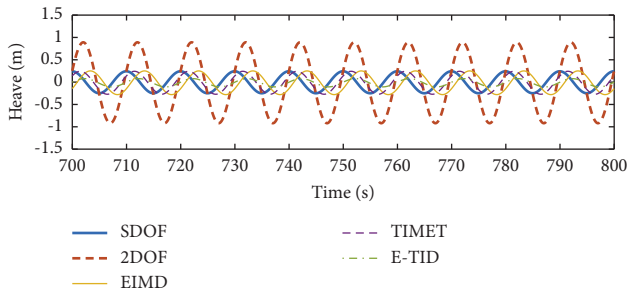
Figure 6: Comparisons of the time histories of Case E for the regular wave of height 6.0 m and period 9.0 s: (a) heave and (b) power.

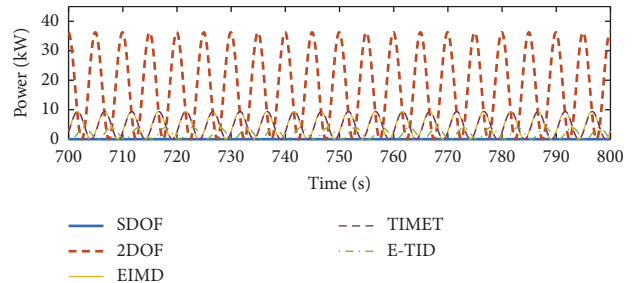Figure 7: Comparisons of the time histories of Case E for the regular wave of height 6.0 m and period 10.0 s: (a) heave and (b) power.

(a)   (b)
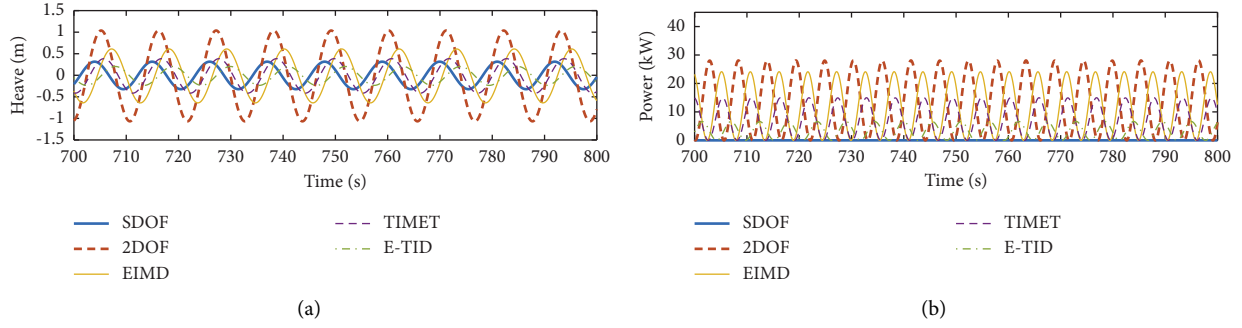
Figure 8: Comparisons of the time histories of Case E for the regular wave of height 6.0 m and period 11.0 s: (a) heave and (b) power.
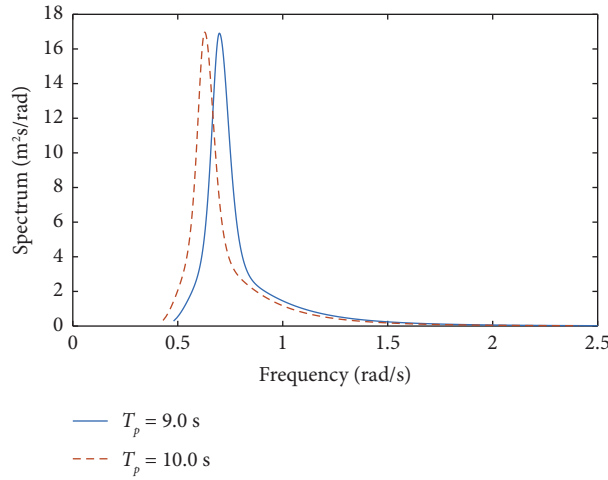

Figure 9: JONSWAP spectrum.

Table 6: Results for the JONSWAP spectrum.

	Case	Heave ($\times 10^{-1}$ m)	Pitch ($\times 10^{-2}$ deg)	Surge ($\times 10^{-1}$ m)	Avg. power (kW)
SDOF		1.22	5.88	2.90	0
2DOF	A, B, and C	3.93	5.81	2.75	5.80
	D, E, and F	3.05	5.81	2.51	4.36
	G, H, and I	2.91	5.99	2.86	5.32
EIMD	A	2.82	6.31	3.06	2.71
	B	2.53	6.25	3.27	2.22
	C	2.35	5.85	3.07	1.63
	D	2.36	6.11	2.85	2.72
	E	2.20	6.11	2.92	2.31
	F	1.92	5.68	2.43	1.50
	G	2.01	5.70	2.32	2.18
	H	1.79	5.83	2.58	1.85
	I	1.65	5.98	2.81	1.74
TIMET	A	1.95	5.78	2.54	2.35
	B	1.61	5.79	2.54	1.87
	C	1.45	5.93	2.85	1.54
	D	1.88	5.71	2.55	2.81
	E	1.70	6.13	2.89	2.66
	F	1.57	5.85	2.90	1.94
	G	1.77	5.81	2.57	2.81
	H	1.80	6.09	3.15	3.25
	I	1.50	5.81	2.51	1.69

TABLE 6: Continued.

	Case	Heave ($\times 10^{-1}$ m)	Pitch ($\times 10^{-2}$ deg)	Surge ($\times 10^{-1}$ m)	Avg. power (kW)
	A	4.40	6.08	3.03	1.19
	B	5.57	5.84	2.39	2.22
	C	1.18	5.81	2.69	1.15
	D	4.14	6.01	2.95	1.40
E-TID	E	4.67	6.26	2.89	2.47
	F	1.24	5.75	2.85	1.52
	G	3.76	5.80	2.59	1.26
	H	4.15	6.10	2.62	2.34
	I	1.31	6.02	2.86	1.77

$H_{1/3}$ = 7.0 m, T_p = 9.0 s, and γ = 5.

TABLE 7: Results for the JONSWAP spectrum.

	Case	Heave ($\times 10^{-1}$ m)	Pitch ($\times 10^{-2}$ deg)	Surge ($\times 10^{-1}$ m)	Avg. power (kW)
SDOF		1.55	9.62	2.93	0
	A, B, and C	4.95	9.36	2.58	6.94
2DOF	D, E, and F	4.50	9.57	2.83	7.54
	G, H, and I	4.08	9.55	3.18	7.28
	A	3.71	9.53	2.71	4.01
	B	3.40	9.58	3.10	3.37
	C	2.95	9.55	2.72	2.37
	D	3.34	9.65	2.71	4.31
EIMD	E	2.98	9.62	2.92	3.80
	F	2.54	9.50	2.88	2.57
	G	3.00	9.65	2.75	4.50
	H	2.66	9.53	2.97	3.88
	I	2.30	9.57	2.83	2.49
	A	3.01	9.53	3.28	5.26
	B	2.18	9.52	2.70	2.57
	C	1.96	9.51	2.62	1.94
	D	2.79	9.74	2.76	4.48
TIMET	E	2.18	9.59	2.79	3.05
	F	1.98	9.45	3.01	2.34
	G	2.67	9.57	2.81	4.25
	H	2.25	9.58	2.85	3.31
	I	2.03	9.66	2.65	2.34
	A	6.60	9.79	2.73	2.12
	B	3.87	9.73	2.75	1.59
	C	4.19	9.56	2.75	1.80
	D	6.15	9.81	2.87	2.58
E-TID	E	3.70	9.61	2.81	2.07
	F	3.70	9.62	2.65	2.00
	G	5.44	9.51	2.58	2.15
	H	3.44	9.67	3.04	2.45
	I	3.39	9.63	2.83	2.38

$H_{1/3}$ = 7.0 m, T_p = 10.0 s, and γ = 4.07.
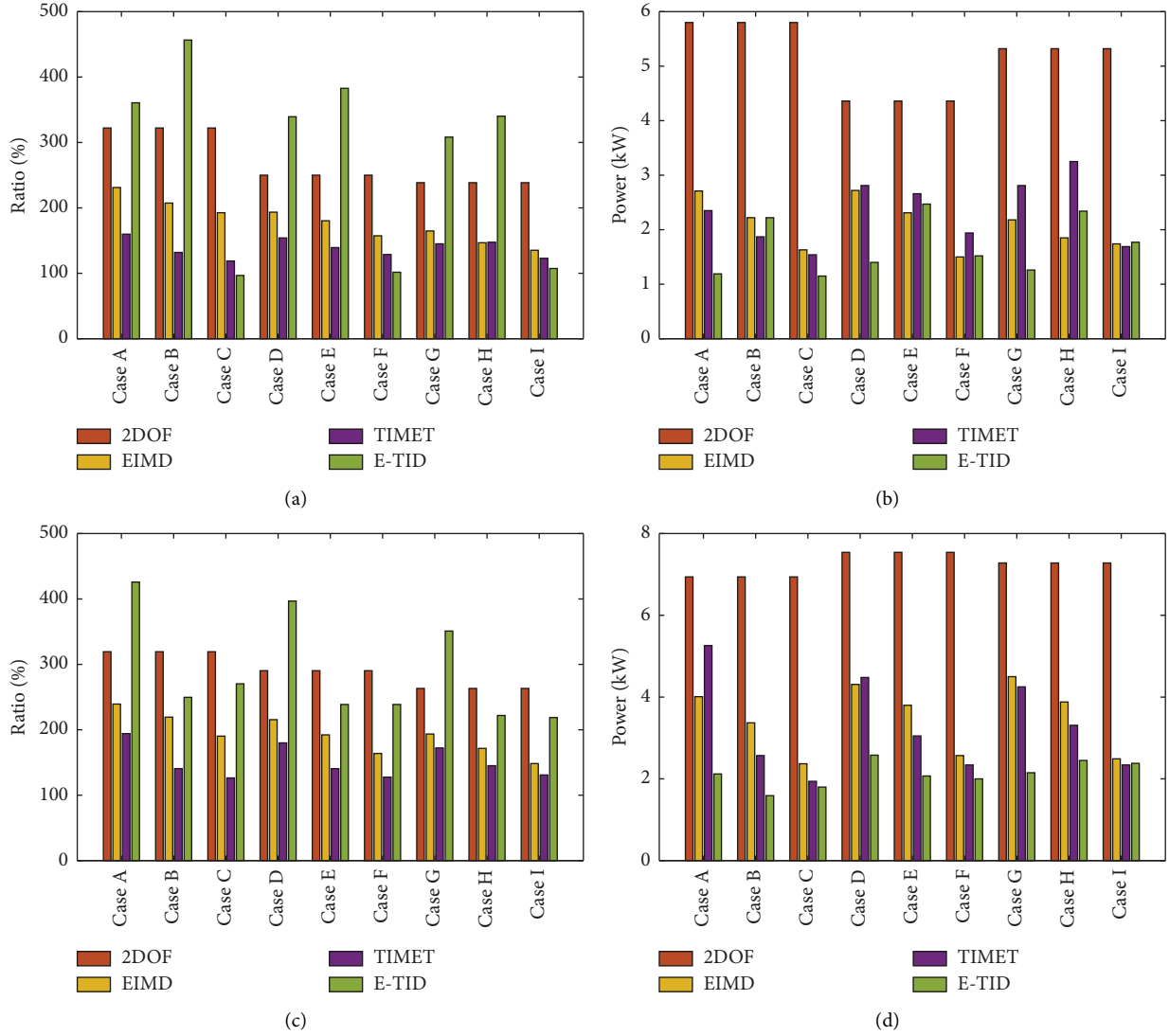
(a)

(b)

(c)

(d)

Figure 10: Comparisons of the RMS heave response ratio to the SDOF model and the average power generation for the irregular waves: (a, b) $H_{1/3}$ = 7.0 m, T_p = 9.0 s, and γ = 5 and (c, d) $H_{1/3}$ = 7.0 m, T_p = 10.0 s, and γ = 4.07.

where $H_{1/3}$ is the significant wave height, f_p is the peak wave frequency (= $1/T_p$), T_p is the peak wave period, f is the wave frequency, and the peak-shape parameter exponent, α, is defined as

$$\alpha = \exp\left[-\left(\frac{f/f_p - 1}{\sqrt{2}\,\sigma}\right)^2\right], \sigma = \begin{cases} 0.07 & \text{for } f \leq f_p, \\ 0.09 & \text{for } f > f_p. \end{cases} \tag{33}$$

The other peak-shape parameter, γ, is determined based on the following equation:

$$\gamma = \begin{cases} 5 & \text{for } \dfrac{T_p}{\sqrt{H_{1/3}}} \leq 3.6, \\[2ex] \exp\left(5.75 - 1.15\dfrac{T_p}{\sqrt{H_{1/3}}}\right) & \text{for } 3.6 < \dfrac{T_p}{\sqrt{H_{1/3}}} \leq 5, \\[2ex] 1 & \text{for } 5 < \dfrac{T_p}{\sqrt{H_{1/3}}}. \end{cases} \tag{34}$$
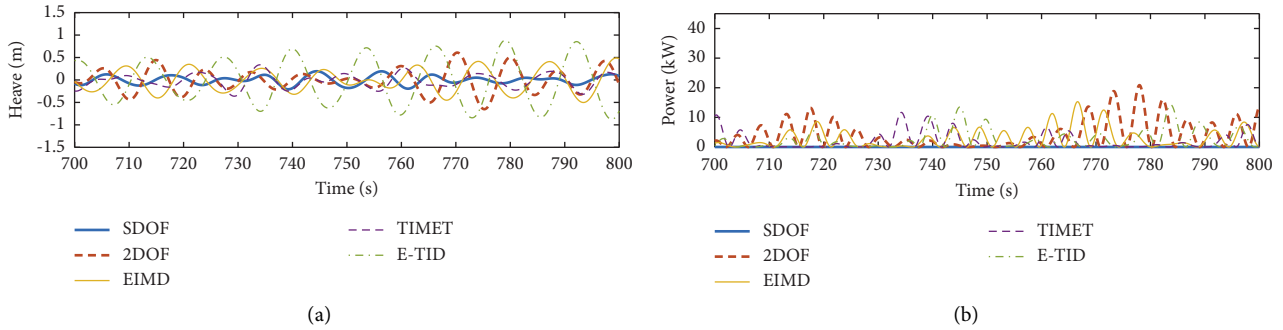
(a)

(b)

FIGURE 11: Comparisons of the time histories of Case E for the JONSWAP spectrum ($H_{1/3}$ = 7.0 m, T_p = 9.0 s, and γ = 5): (a) heave and (b) power.
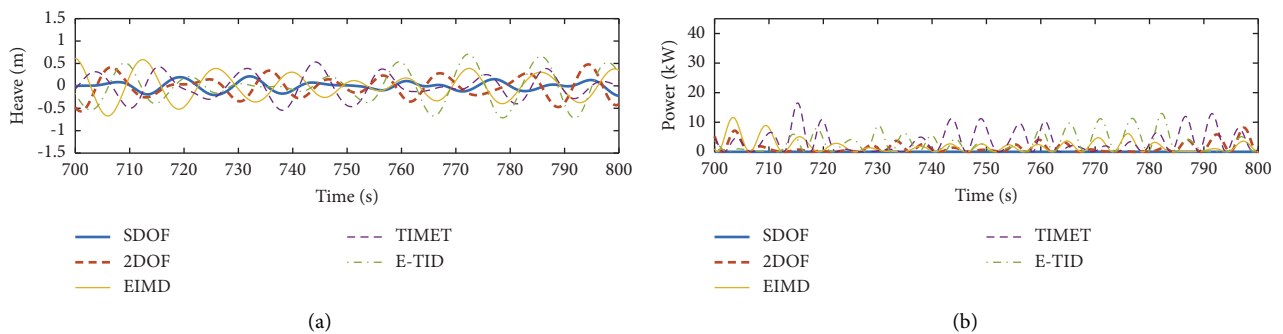

(a)

(b)

FIGURE 12: Comparisons of the time histories of Case E for the JONSWAP spectrum ($H_{1/3}$ = 7.0 m, T_p = 10.0 s, and γ = 4.07): (a) heave and (b) power.

In this study, two irregular waves produced by the abovementioned equations are used as JONSWAP spectrum waves. The first one has a significant wave height of 7.0 m and a peak wave period of 9.0 s, and the second one has a significant wave height of 7.0 m and a peak wave period of 10.0 s. The peak-shape parameter, γ, of each case becomes 5 and 4.07, respectively, from equation (34). The spectra of these two JONSWAP waves are compared in Figure 9, which shows that the JONSWAP spectrum contains broadband waves.

In the same way as with the regular waves, the RMS responses and average power are summarized in Tables 6 and 7, the heave response ratio and power generation are compared in Figure 10, and the time histories of the heave response and power generation are shown in Figures 11 and 12. As can be seen, the proposed systems utilizing the inerter-based PTO systems deteriorate the heave response in most cases compared to the SDOF model. This is because the irregular waves contain the waves in the period range where the PTO system does not suppress the heave response, as shown in Figure 3. Particularly, the E-TID did not work at all to the waves with a peak wave period of 10.0 s due to the long-period or low-frequency wave components included in the JONSWAP spectrum. However, considering the additional benefit of the WEC and the fact that the heave response does not deteriorate significantly, the EIMD and the TIMET still have sufficient advantages over the

conventional floating OWT even to waves containing broadband components.

4. Conclusions

This article introduced the novel floating OWT coupled with inerter-based PTO systems. To investigate the effectiveness, the three well-known configurations of the electromagnetic inerter-based devices, i.e., EIMD, TIMET, and E-TID, were applied to the PTO system for the spar-type floating OWT separated into two parts. Numerical simulation studies implemented in WEC-Sim showed that the inerter-based PTO systems worked well on the present floating OWT to improve its structural vibration suppression in the heave direction and wave energy harvesting capabilities when the parameters of the PTO systems were appropriately designed for the particular incident wave period. In other words, the performance was highly dependent on the incident wave period and the inertance value; thus, it was observed that the proposed system had a risk of deteriorating the structural control performance for waves with unexpected periods.

To address this issue, not only optimal design methods for the present OWT but also variable inerter mechanisms, which can change the inertance value, should be developed and applied to the inerter-based PTO systems for future work. This improvement is especially necessary for the E-TID, which is sensitive to the inertance value. In addition, to control both inertance value and damping coefficient of the

PTO system for better performance, algorithms based on feedback control strategies using the measured wave data on-site to adapt the change of the dominant period of the incident waves should be developed. Moreover, other types of floating OWTs such as semisubmersible type should be used for the proposed inerter-based PTO systems, and their structural control performance in the pitch and surge directions when not only waves but also wind loadings are applied should be evaluated as well. Finally, experimental verification is also necessary to show the efficacy of the proposed systems and find out practical difficulties.

Data Availability

The simulation data used to support the findings of this study are available from the corresponding author upon request.

Conflicts of Interest

The authors declare that they have no conflicts of interest.

Acknowledgments

References

[1] A. R. Henderson, C. Morgan, B. Smith, H. C. Sørensen, R. J. Barthelmie, and B. Boesmans, "Offshore wind energy in europe— a review of the state-of-the-art," *Wind Energy*, vol. 6, no. 1, pp. 35–52, 2003.

[2] M. D. Esteban, J. J. Diez, J. S. López, and V. Negro, "Why offshore wind energy?" *Renewable Energy*, vol. 36, no. 2, pp. 444–450, 2011.

[3] X. Sun, D. Huang, and G. Wu, "The current state of offshore wind energy technology development," *Energy*, vol. 41, no. 1, pp. 298–312, 2012.

[4] J. Kaldellis and M. Kapsali, "Shifting towards offshore wind energy—recent activity and future development," *Energy Policy*, vol. 53, pp. 136–148, 2013.

[5] M. C. Smith, "The inerter: a retrospective," *Annual Review of Control, Robotics, and Autonomous Systems*, vol. 3, no. 1, pp. 361–391, 2020.

[6] R. Ma, K. Bi, and H. Hao, "Inerter-based structural vibration control: a state-of-the-art review," *Engineering Structures*, vol. 243, Article ID 112655, 2021.

[7] M. C. Smith, "Synthesis of mechanical networks: the inerter," *IEEE Transactions on Automatic Control*, vol. 47, no. 10, pp. 1648–1662, 2002.

[8] Y. Hu, J. Wang, M. Z. Chen, Z. Li, and Y. Sun, "Load mitigation for a barge-type floating offshore wind turbine via inerter-based passive structural control," *Engineering Structures*, vol. 177, pp. 198–209, 2018.

[9] M. A. Lackner and M. A. Rotea, "Passive structural control of offshore wind turbines," *Wind Energy*, vol. 14, no. 3, pp. 373–388, 2011.

[10] Z. Zhang and B. Fitzgerald, "Tuned mass-damper-inerter (TMDI) for suppressing edgewise vibrations of wind turbine blades," *Engineering Structures*, vol. 221, Article ID 110928, 2020.

[11] S. Sarkar and B. Fitzgerald, "Vibration control of spar-type floating offshore wind turbine towers using a tuned mass-damper-inerter," *Structural Control and Health Monitoring*, vol. 27, no. 1, Article ID e2471, 2020.

[12] S. Sarkar and B. Fitzgerald, "Fluid inerter for optimal vibration control of floating offshore wind turbine towers," *Engineering Structures*, vol. 266, Article ID 114558, 2022.

[13] Z. Zhang and C. Høeg, "Inerter-enhanced tuned mass damper for vibration damping of floating offshore wind turbines," *Ocean Engineering*, vol. 223, Article ID 108663, 2021.

[14] R. Ma, K. Bi, and H. Hao, "Mitigation of heave response of semi-submersible platform (SSP) using tuned heave plate inerter (THPI)," *Engineering Structures*, vol. 177, pp. 357–373, 2018.

[15] R. Ma, K. Bi, and H. Hao, "Heave motion mitigation of semi-submersible platform using inerter-based vibration isolation system (IVIS)," *Engineering Structures*, vol. 219, Article ID 110833, 2020.

[16] Y. Nakamura, A. Fukukita, K. Tamura et al., "Seismic response control using electromagnetic inertial mass dampers," *Earthquake Engineering & Structural Dynamics*, vol. 43, no. 4, pp. 507–527, 2014.

[17] H. Zhu, Y. Li, W. Shen, and S. Zhu, "Mechanical and energy-harvesting model for electromagnetic inertial mass dampers," *Mechanical Systems and Signal Processing*, vol. 120, pp. 203–220, 2019.

[18] T. Asai, Y. Araki, and K. Ikago, "Energy harvesting potential of tuned inertial mass electromagnetic transducers," *Mechanical Systems and Signal Processing*, vol. 84, pp. 659–672, 2017.

[19] K. Sugiura, Y. Watanabe, T. Asai, Y. Araki, and K. Ikago, "Experimental characterization and performance improvement evaluation of an electromagnetic transducer utilizing a tuned inerter," *Journal of Vibration and Control*, vol. 26, no. 1-2, pp. 56–72, 2020.

[20] A. Gonzalez-Buelga, L. R. Clare, S. A. Neild, J. Z. Jiang, and D. J. Inman, "An electromagnetic inerter-based vibration suppression device," *Smart Materials and Structures*, vol. 24, no. 5, Article ID 055015, 2015.

[21] R. Haraguchi and T. Asai, "Enhanced power absorption of a point absorber wave energy converter using a tuned inertial mass," *Energy*, vol. 202, Article ID 117740, 2020.

[22] K. Sugiura, R. Sawada, Y. Nemoto, R. Haraguchi, and T. Asai, "Wave flume testing of an oscillating-body wave energy converter with a tuned inerter," *Applied Ocean Research*, vol. 98, Article ID 102127, 2020.

[23] T. Asai and K. Sugiura, "Numerical evaluation of a two-body point absorber wave energy converter with a tuned inerter," *Renewable Energy*, vol. 171, pp. 217–226, 2021.

[24] Y. Nemoto, M. Takino, S. Tsukamoto, and T. Asai, "Numerical study of a point absorber wave energy converter with tuned variable inerter," *Ocean Engineering*, vol. 257, Article ID 111696, 2022.

[25] M. Kamarlouei, J. Gaspar, M. Calvario et al., "Experimental analysis of wave energy converters concentrically attached on a floating offshore platform," *Renewable Energy*, vol. 152, pp. 1171–1185, 2020.

[26] J. Gaspar, M. Kamarlouei, F. Thiebaut, and C. Guedes Soares, "Compensation of a hybrid platform dynamics using wave energy converters in different sea state conditions," *Renewable Energy*, vol. 177, pp. 871–883, 2021.

[27] M. J. Muliawan, M. Karimirad, T. Moan, and Z. Gao, "STC (Spar-Torus combination): a combined spar-type floating wind turbine and large point absorber floating wave energy

converter promising and challenging," *Ocean Space Utilization; Ocean Renewable Energy of International Conference on Offshore Mechanics and Arctic Engineering*, vol. 7, pp. 667–676, 2012.

[28] M. J. Muliawan, M. Karimirad, and T. Moan, "Dynamic response and power performance of a combined Spar-type floating wind turbine and coaxial floating wave energy converter," *Renewable Energy*, vol. 50, pp. 47–57, 2013.

[29] L. Wan, Z. Gao, T. Moan, and C. Lugni, "Experimental and numerical comparisons of hydrodynamic responses for a combined wind and wave energy converter concept under operational conditions," *Renewable Energy*, vol. 93, pp. 87–100, 2016.

[30] Z. Cheng, T. R. Wen, M. C. Ong, and K. Wang, "Power performance and dynamic responses of a combined floating vertical axis wind turbine and wave energy converter concept," *Energy*, vol. 171, pp. 190–204, 2019.

[31] J. Hu, B. Zhou, C. Vogel et al., "Optimal design and performance analysis of a hybrid system combing a floating wind platform and wave energy converters," *Applied Energy*, vol. 269, Article ID 114998, 2020.

[32] C. Michailides, Z. Gao, and T. Moan, "Experimental study of the functionality of a semisubmersible wind turbine combined with flap-type Wave Energy Converters," *Renewable Energy*, vol. 93, pp. 675–690, 2016.

[33] J. Sarmiento, A. Iturrioz, V. Ayllón, R. Guanche, and I. Losada, "Experimental modelling of a multi-use floating platform for wave and wind energy harvesting," *Ocean Engineering*, vol. 173, pp. 761–773, 2019.

[34] Y. Si, Z. Chen, W. Zeng et al., "The influence of power-take-off control on the dynamic response and power output of combined semi-submersible floating wind turbine and point-absorber wave energy converters," *Ocean Engineering*, vol. 227, Article ID 108835, 2021.

[35] H. R. Ghafari, H. Ghassemi, and G. He, "Numerical study of the Wavestar wave energy converter with multi-point-absorber around DeepCwind semisubmersible floating platform," *Ocean Engineering*, vol. 232, Article ID 109177, 2021.

[36] K. Ruehl, D. Ogden, Y. H. Yu et al., "WEC-Sim v5.0.1," 2022, https://zenodo.org/record/7121186.

[37] J. Jonkman, S. Butterfield, W. Musial, and G. Scott, "Definition of a 5-MW reference wind turbine for offshore system development," Tech. Rep. NREL/TP-500-38060, National Renewable Energy Laboratory, Golden, CO, USA, 2009.

[38] J. Jonkman, "Definition of the floating system for phase IV of OC3," Tech. Rep. NREL/TP-500-47535, National Renewable Energy Laboratory, Golden, CO, USA, 2010.

[39] J. Newman and J. Grue, *Marine Hydrodynamics*, The MIT Press, Cambridge, MA, USA, 40th edition, 2018.

[40] Wamit Inc, "Wamit," 2023, https://www.wamit.com/index.htm.

[41] I. Cassidy, J. Scruggs, S. Behrens, and H. P. Gavin, "Design and experimental characterization of an electromagnetic transducer for large-scale vibratory energy harvesting applications," *Journal of Intelligent Material Systems and Structures*, vol. 22, no. 17, pp. 2009–2024, 2011.

[42] Matlab Simulink, *The MathWorks*, MATLAB/SIMULINK, Simulink, MA, USA, 2023.

[43] O. M. Faltinsen, *Sea Loads on Ships and Offshore Structures*, Cambridge University Press Cambridge, New York, NY, USA, 1990.

[44] J. Song, K. Bi, R. Ma, K. Xu, and Q. Han, "Optimum design and performance evaluation of inerter-based dampers for seismic protection of adjacent bridges," *Structures*, vol. 55, pp. 1277–1291, 2023.